Biosensors and Bioelectronics 170 (2020) 112598

Contents lists available at ScienceDirect

Biosensors and Bioelectronics

journal homepage: http://www.elsevier.com/locate/bios

Highly sensitive label-free electrochemical aptasensors based on photoresist derived carbon for cancer biomarker detection

Shahrzad Forouzanfar [a,*], Fahmida Alam [a], Nezih Pala [a], Chunlei Wang [b,**]

[a] Department of Electrical and Computer Engineering, Florida International University, United States
[b] Department of Mechanical and Materials Engineering, Florida International University, United States

ARTICLE INFO

Keywords:
Cancer biomarker
Label-free
Electrochemical
Carbon
Aptamer
PDGF-BB

ABSTRACT

-Label-free electrochemical aptasensors for cancer biomarker detection can be a promising means for early detection of cancer due to their high sensitivity, selectivity, and stability, and low cost. In this study, a highly sensitive and selective label-free electrochemical aptasensor based on carbon microelectromechanical systems (C-MEMS) was developed for the detection of platelet-derived growth factor-BB (PDGF-BB). The active electrodes of the aptasensors were synthesized via carbonization of SU-8 derived electrodes at high temperatures in an oxygen-free furnace. An oxygen-plasma oxidation treatment was used to functionalize the C-MEMS electrodes, which provided efficient covalent immobilization of amino terminated affinity aptamers. The turn-off and turn-on detection strategies–based on capacitance and resistance measurement, respectively—were employed. The capacitance detection strategies exhibited a wide linear response range of 0.01–50 nM, with a high sensitivity of 3.33 mF cm-2 Logc-1 (unit of c, nM) and a low limit of detection of 7 pM (S/N = 3). The resistance detection strategies exhibited an even wider linear response range of 0.005–50 nM, and a lower limit of detection of 1.9 pM (S/N = 3), with a high sensitivity of 1.65 × 103 Ω $Logc^{-1}$ (unit of c, nM). Both detection strategies provided high selectivity for PDGF-BB and high stability of 90.34% after 10 days. This research demonstrates that the developed label-free electrochemical C-MEMS based PDGF-BB aptasensor is highly sensitive, selective, and robust. This aptasensor is a promising prospect for the highly demanding task of early detection of cancer biomarkers.

1. Introduction

Cancer is the second major cause of death worldwide, being responsible for an estimated 9.6 million deaths in 2019(WHO, 2020). Many cancer patients have a high chance of being cured if they are diagnosed early(WHO, 2020). An effective means to early cancer diagnosis is quantifying the number of cancer biomarkers collected from biofluids like blood and urine(Chatterjee and Zetter, 2005). Platelet-derived growth factor-BB (PDGF-BB) is a biomarker detectable in blood which plays a crucial role in solid malignant tumor development and lymphatic metastasis(Cao et al., 2004). Several studies have investigated the potential contribution of PDGF-BB in malignant tumors such as breast cancer(Yi et al., 2002), pancreatic cancer(Kawaguchi et al., 2012), prostate cancer(Cheng et al., 2013), ovarian cancer(Cimpean et al., 2016), and liver cancer(Lau et al., 2009). There exists no Food and Drug Administration (FDA) guidance on the normal range of PDGF-BB in human plasma; however, the 0.1–1.5 ng mL^{-1} is widely considered to be a normal range(Kajizuka et al., 2010). The concentration of this biomarker can vary vastly in different cancers; for instance, PDGF-BB concentration above 42 ng mL^{-1} (the equivalent of 1.72 nM) is reported for patients with lung cancer(Ma et al., 2020). The role of PDGF-BB in the development of various cancerous tumors illustrates the importance of developing accurate and affordable point-of-care (POC) PDGF-BB cancer biomarker sensors suitable for the diagnosis of cancerous tumors at early stages.

Synthetic affinity RNA and DNA based bio-recognizers—commonly referred to as aptamers—have attracted considerable attention for developing cancer biosensors. Aptamers have various advantages that make them suitable for this purpose: the production of aptamers is highly repeatable; modifying aptamers (e.g., chemical modifications or attaching optical tags) is simpler than modifying antibodies; and aptamers show less non-specific detection phenomena than other bio-receptors(Willner and Zayats, 2007). Various mechanisms can be used for POC label-free aptamer-based biosensors (i.e., aptasensors),

* Corresponding author.
** Corresponding author. Tel.: (305) 348-1217.
E-mail addresses: sforo003@fiu.edu (S. Forouzanfar), wangc@fiu.edu (C. Wang).

https://doi.org/10.1016/j.bios.2020.112598
Received 24 July 2020; Received in revised form 2 September 2020; Accepted 4 September 2020
Available online 18 September 2020

including optical, piezoelectric (i.e., mass-spectroscopy), and electrochemical detection strategies(Forouzanfar et al., 2020b). Optical aptasensors can offer extremely low limits of detection and high signal-to-noise ratios. However, they have some critical drawbacks, such as the need for complicated labeling processes and complicated optical analysis tools for obtaining output signals, and limitations in providing stable surface functionalization for aptamers immobilization (Prasad et al., 2019). Mass-spectroscopy (MS) can offer extremely accurate measurements; however, there are technical considerations associated with using MS, which reduce its feasibility for on-site and POC applications. For instance, MS machines require a specific footprint area on each side, as well as complicated analysis tools; the high sensitivity of this technique to surrounding conditions—which necessitates the use of specific heat and ventilation systems—is another complication related to MS measurements(Jannetto, 2017; Pei et al., 2020). Electrochemical aptasensors are highly suitable for POC applications since they possess several advantages over other types of aptasensors. For instance, the electrochemical parameters can be measured without utilizing labels (i.e., label-free detection), in which label-free detection refers to the process of eliminating foreign molecules (e.g., fluorescents tags, chemiluminescent, and nanoparticle) that are temporarily or chemically attached to the target of interest, in order to detect its presence or activity(Syahir et al., 2015; Zhang et al., 2019). Electrochemical aptasensors can also be efficiently miniaturized and integrated with lab-on-chip devices and complementary metal–oxide–semiconductor (i.e., CMOS) circuits. The price of electrochemical sensing units can be considerably reduced (e.g., paper-based electrochemical sensing electrodes)(Wang et al., 2019). Moreover, label-free electrochemical detection can reduce the cost of operation and blood sample consumption by requiring relatively simple sample preparation(Cui et al., 2018; Forouzanfar et al., 2015; Ma et al., 2019; Ranjan et al., 2017). However, the sensing performance of label-free electrochemical aptasensors such as sensitivity, selectivity, and dynamic range requires further enhancements to match the performance of the clinical test.

Recently, several studies have reported highly sensitive label-free electrochemical aptasensors for PDGF-BB detection. For example, Jiang et al. have developed amperometric aptasensors based on hydroxyapatite nanoparticles deposited on a glassy carbon electrode with the amperometric signal linear in the range of 0.1 pg mL^{-1}-10 ng mL^{-1} PDGF-BB concentration(Jiang et al., 2017). Zhang et al. introduced a sensing probe based on graphene enhanced with sliver nanoclusters that showed a linear range toward PDGF-BB from 32.3 fM–16.61 pM(Zhang et al., 2017). However, in most published studies, the linear range is narrower than the required linear range for cancer diagnosis purposes. For instance, PDGF-BB concentrations higher than 42 ng mL^{-1} (the equivalent of 1.72 nM) have been discovered in serum samples of lung cancer patients(Ma et al., 2020). Hence, further studies are required to improve the performance (especially the detection range) of label-free electrochemical PDGF-BB aptasensors and make them more feasible for mass production.

Carbon-based microelectrochemical devices (C-MEMS) are glassy-carbon devices derived from pyrolyzed epoxy-based photoresist (i.e., SU-8 photoresist) at high temperatures in oxygen-free environments. C-MEMS-based electrodes possess features that make them highly suitable for biosensing applications such as good conductivity, high physiochemical stability, wide electrochemical windows, high tolerance against biofouling phenomenon, and highly accessible surface functionalization(Adelowo et al., 2020; Ferrer-Argemi et al., 2018; Piñón et al., 2017; Wang and Madou, 2005). The surfaces of C-MEMS-based electrodes can be functionalized with carboxyl functional groups using vacuum ultraviolet, electrochemical activation, and oxygen reactive ion etching (RIE) (Forouzanfar et al., 2020a; Penmatsa et al., 2014). The C-MEMS synthesis technique can produce electrodes with high resolution (i.e., tens of nanometers) and good yields of fabrication, which are highly favorable for POC applications(Wang and Madou, 2005). Nano-enabled C-MEMS electrodes enhance aptamer immobilization efficiency (i.e., by providing a larger accessible surface area), and highly accessible functionalization promotes the stability of the aptasensor by providing covalent immobilization of the aptamers.

In this work, we demonstrate label-free electrochemical PDGF-BB aptasensors based on thin layer (designated as ThL) electrodes fabricated via the C-MEMS synthesis procedure and PDGF-BB binding DNA aptamers. The designation “thin layer” refers to the single layer of

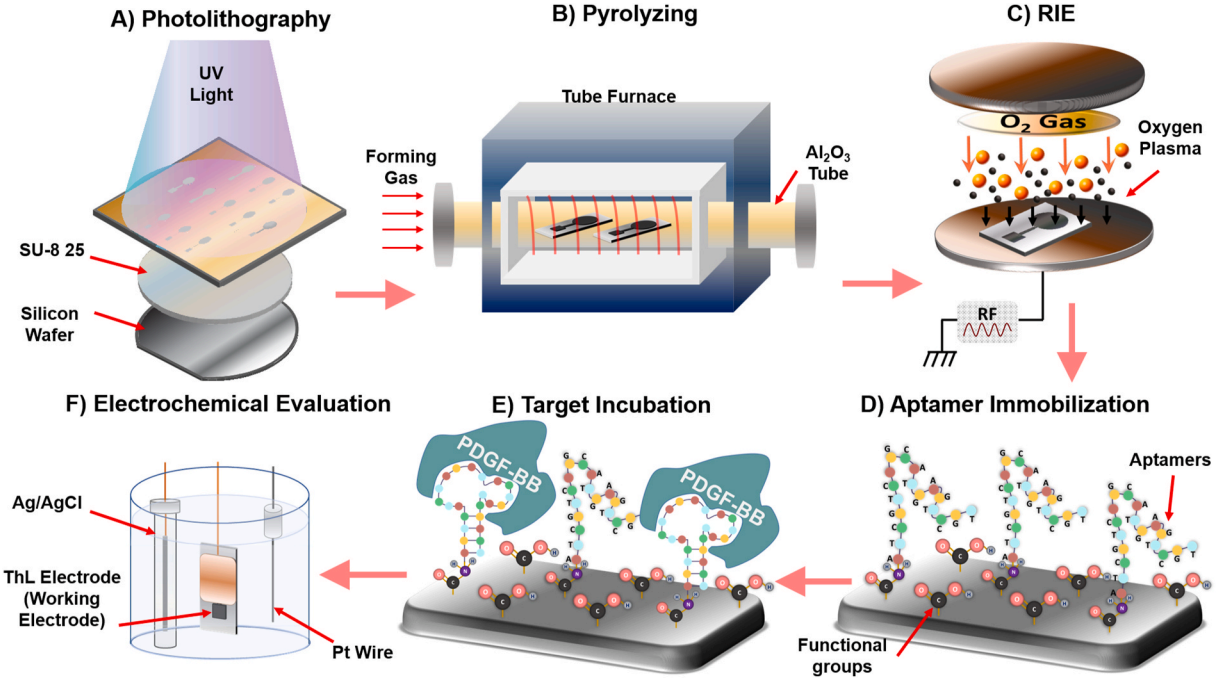

Fig. 1. Schematic illustration of the fabrication process of the C-MEMS based PDGF-BB aptasensor and electrochemical test cell with 5 mL aqueous electrolytes based on a mixture of 5 mM $k_3Fe(CN)_6$ and 0.1 M PBS with various concentrations of KCl ranging from 50 mM to 1 M.

photoresist-derived carbon without additional 3-dimensional features such as micropillars. The ThL electrodes were pretreated with oxygen plasma oxidation treatment to form –COOH functional groups on their surfaces, onto which amino-group-modified affinity aptamers were immobilized directly. Fourier-transform infrared spectroscopy (FTIR) was used to study the surface characteristics of the fabricated C-MEMS electrodes. Cyclic voltammetry (CV) and electrochemical impedance spectroscopy (EIS) were used to optimize the fabrication parameters and analyze the performance of the aptasensors. The results demonstrate that the developed ThL-based PDGF-BB aptasensors are highly sensitive, selective, stable, and robust, and have a sufficiently broad dynamic range compared to previously reported label-free electrochemical PDGF-BB aptasensors. Furthermore, the C-MEMS technique is both feasible and amenable to mass production, thus making C-MEMS based PDGF-BB aptasensors promising for further enhanced cancer diagnosis and monitoring POC microdevices.

2. Materials and methods

2.1. Materials and reagents

The PDGF-BB binding aptamer (ssDNA, amino linker-5′-C_6-CAG GCT ACG GCA CGT AGA GCA TCA CCA TGA TCC TG-3' (Forouzanfar et al., 2020b)) was purchased in HPLC purification from ThermoFisher Scientific, USA. Tris-ethylenediaminetetraacetic acid (TE) buffer, ethanol, acetone, phosphate-buffered saline (1M and pH 7.4) (PBS), 1-ethyl-3-(3-dimethylaminopropyl) carbodiimide hydrochloride linker (EDC), N-hydroxysuccinimide linker (NHS), hydrochloric acid (HCl), Polyoxyethylene (20) sorbitan monolaurate (Tween-20), KCl, and $k_3Fe(CN)_6$ were purchased from ThermoFisher Scientific, USA. Trehalose, bovine serum albumin (BSA), and platelet-derived growth factor-AA, AB, and BB were purchased from Sigma Aldrich, USA. NANO™ SU-8 25 negative photoresist was purchased from Microchem., USA. All chemicals were analytical grade. Milli-Q (Sigma Aldrich, USA) deionized water (DI water) was used in this study.

2.2. Apparatus

Plasma-oxidation treatment was conducted using the MARCH CS-1217 reactive ion etch (RIE) system. All electrochemical characterizations were conducted using a Bio-Logic versatile multichannel potentiostat (VMP3) at room temperature. A three-electrode cell—which included a ThL electrode as the working electrode, a platinum wire as a counter electrode, and Ag/AgCl (KCl saturated) as a reference electrode—was used for all electrochemical measurements. A 713 Metrohm pH meter was used for measuring the pH of electrolytes. FTIR analysis was conducted using a JASCO FTIR 4100 equipped with an attenuated total reflectance ATR accessory to verify –COOH carboxylic group and other functional groups on the sensor surfaces.

2.3. Fabrication of ThL electrodes

The ThL electrodes were fabricated via the previously reported C-MEMS synthesis process(Wang et al. 2004, 2005), which is schematically illustrated in Fig. 1A and B. The fabrication process started with cleaning a 4-inch p-doped single-side polished silicon wafer with acetone and methanol. A layer of SU-8 25 photoresist was spin-coated on the wafer at 300 rpm for 10 s and then accelerated to 3000 rpm for 30 s to provide a uniform photoresist layer with a thickness of approximately 15 μm. Soft bakes at 65 °C for 3 min and 95 °C for 7 min were conducted on hotplates, followed by UV light exposure with a dose of 300 mJ cm^{-2}. Post-exposure bakes were conducted at 65 °C for 1 min and 95 °C for 5 min on hotplates. The electrodes were pyrolyzed in a Lindenberg tube furnace with a temperature ramp of 10 °C min^{-1} in two steps of 250 °C with a dwell time of 30 min, and 900 °C with a dwell time of 60 min, under 500 sccm flow of forming gas ($5\%H_2 + 95\%N_2$). The samples were left in the furnace overnight to cool to room temperature.

2.4. Preparation of PDGF-BB aptasensors

The ThL electrodes were functionalized using oxygen-plasma oxidation conducted in the RIE system illustrated in Fig. 1C. Oxygen flow of 60 mL min^{-1} at 400 mTorr pressure and RF power of 100 W were used for functionalization. The optimum etching time was chosen as 7 min based on previous studies(Penmatsa et al., 2014). The oxygen plasma-treated electrode (designated as ThL_{RIE}), was washed thoroughly in 1 M PBS for 5 min and DI water for 3 min before the next preparation steps.

The aptamer stock solutions were prepared based on the suggested procedure in the datasheet released by ThermoFisher Scientific for oligonucleotide preparation and storage. The diluted stocks were prepared in 0.1 M TE buffer with a final volume of 10 μL. Before immobilizing aptamers, 5 μL of 20 mg mL^{-1} EDC and 10 μL of 20 mg mL^{-1} NHS were added to the aptamer solution with the desired concentration ranging from 50 nM to 15 μM. The aptamer solution was incubated for 30 min at room temperature. This step is recommended for activating the amino linker tags of the aptamers. The prepared aptamer solution was deposited on the ThL_{RIE} electrode surfaces and followed by incubation for 2 h at room temperature. After incubation, electrodes were washed thoroughly in DI water to wash any unattached aptamers. In order to quench blank areas of the ThL electrodes, 50 μL of the aqueous solution of 0.1 M PBS +1% (v:v) Tween-20 was deposited on the electrodes and followed by incubation for 10 min. The aptamer immobilized electrodes (designated as $ThL_{RIE+Apt}$) (Fig. 1D) were washed with DI water for 5 min and stored in 0.1 M TE buffer in the refrigerator (4 °C) when not in use.

2.5. Electrochemical characterization of PDGF-BB aptasensors

The stock solutions of PDGF-AA, AB, and BB were prepared based on the suggested procedure in the datasheet released by Sigma Aldrich. The samples were diluted in an aqueous solution of DI water and 5% (v:v) trehalose to a final volume of 15 μL. The desired target was added to the ThL electrodes and followed by incubation at room temperature (25 °C) for between 10 and 150 min. The optimum time for reaction of target molecules with binding aptamers was found to be 40 min. Following target immobilization, which is schematically illustrated in Fig. 1E, the ThL electrodes were washed in DI water before electrochemical measurements were conducted. The electrodes incubated with the target were immediately tested via the three-electrode setup illustrated in Fig. 1F for CV and EIS evaluations. The 5 mL aqueous electrolytes—based on a mixture of 5 mM $k_3Fe(CN)_6$ and 0.1 M PBS with various concentrations of KCl ranging from 50 mM to 1 M—were used for electrochemical measurements. In CV measurements, ThL electrodes were tested between −0.2 V and 0.6 V versus reference electrode with scan rates of 10–120 mV s^{-1}. All CV data were typically taken after conducting 20 continuous cycles to ensure a reliable data recording. EIS measurements were recorded at a frequency range of 10–250,000 Hz and at various potentials including open-circuit potential (E_{OC}), 0.15, 0.2, and 0.35 V (vs. Ag/AgCl). The pH of the electrolyte was adjusted using HCl to achieve electrolytes with a pH of 7.4–4.0. The optimum pH of 6.5 was used for sensing performance characterizations. After every electrochemical measurement, the C-MEMS aptasensors were regenerated by immersing the sensing electrodes in 1 M TE buffer with gentle stirring for 30 min. All of the target incubations and electrochemical tests were conducted at room temperature (25 °C).

3. Results and discussion

In the PDGF-BB detection experiments, PDGF-BB binding aptamers modified with amino-linker tags were used as bio-recognizers. The FTIR and electrochemical characterization were conducted on three types of

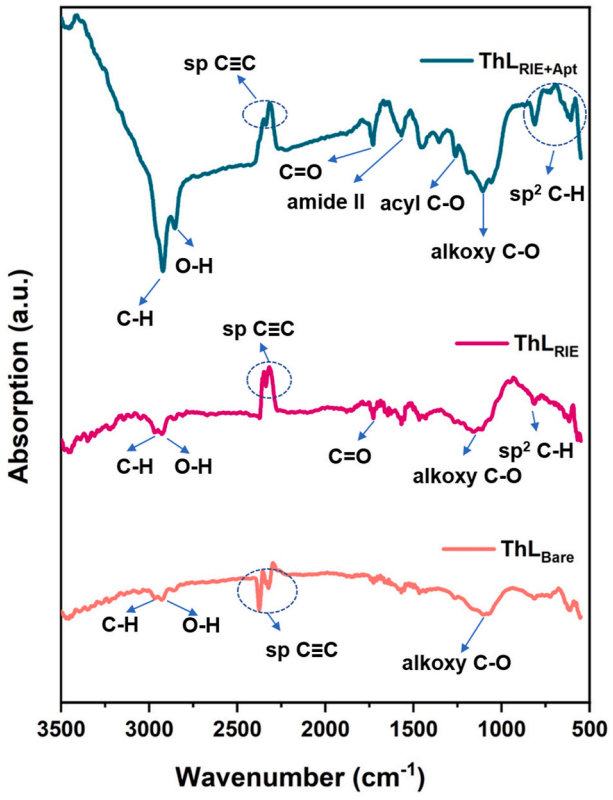

Fig. 2. FTIR spectra of ThL_{Bare}, ThL_{RIE}, and $ThL_{RIE+Apt}$ electrodes.

C-MEMS thin layer (designated as ThL) electrodes samples referred to as ThL_{Bare}, ThL_{RIE}, and $ThL_{RIE+Apt}$, which they represent the C-MEMS electrodes without any modifications, after RIE functionalization, and after immobilizing aptamers, respectively. The 2.5 μM aptamer concentration was used in the fabrication of $ThL_{RIE+Apt}$ studied in subsections 3.1, 3.2, and 3.3, with an exception for $ThL_{RIE+Apt}$ electrodes prepared to study the effect of aptamer concentration. The optimum aptamer concentration of 7.5 μM was used for the fabrication of $ThL_{RIE+Apt}$ electrodes studied in subsections 3.4 and 3.5. The active area of 5 × 5 mm^2 in all C-MEMS electrodes was confined using bee's wax to minimize side reactions. The 5 mM of $K_3Fe(CN)_6$ was used as a redox agent.

Two electrochemical measurement strategies of EIS and CV were used for analytical purposes. The Faradaic mode of EIS was conducted at the oxidation potential of $Fe(CN)_6^{-3/-4}$ and non-Faradaic mode of EIS was conducted at $E = E_{OC}$ to measure the charge-transfer resistance and double-layer capacitance, respectively. The CV measurements were conducted at a scan rate of 50 mV s^{-1} unless otherwise mentioned (i.e., in studies on the effect of scan rates presented in subsection 3.2). The areal capacitances were calculated from CV curves using Eq. (1) (Frackowiak, 2007):

$$C = \frac{1}{2AsΔV} \int IdV \quad (1)$$

Where A is the electrode area, s is scan rate, $ΔV$ is the voltage window, I is current, and V is voltage. It is worth mentioning that the sample size (i.e., n) in this article refers to the number of repeated tests on each measurement point, which varies between 3 and 20 throughout the measurements presented herein.

3.1. FTIR characterization of ThL electrodes

The FTIR characterization was used to confirm the formation of carboxylic groups during the functionalization and immobilization of affinity aptamers via amide binding on the surfaces of the C-MEMS electrodes. The FTIR spectra of ThL_{Bare}, ThL_{RIE}, and $ThL_{RIE+Apt}$ are represented in Fig. 2. All three samples showed two peaks between 2800 and 3000 cm^{-1} and two peaks between 2300 and 2400 cm^{-1}, which are attributed to OH and sp C–H stretching, and sp C≡C bending, respectively(Choi et al., 2010). Furthermore, ThL_{RIE} showed a peak at 823 cm^{-1}, and $ThL_{RIE+Apt}$ showed two peaks at 607 cm^{-1} and 819 cm^{-1}, which are attributed to sp^2 C–H bending(Choi et al., 2010).

The spectrum of the ThL_{Bare} showed a peak at 1110 cm^{-1}, which is assigned to alkoxy C–O(Coates, 2006). This peak is the result of native oxidation of carbon in contact with air. The FTIR spectrum of ThL_{RIE} and $ThL_{RIE+Apt}$ exhibited the same peak around 1155 and 1105 cm^{-1}, respectively. The FTIR of ThL_{RIE} also showed a peak at 1251 cm^{-1}, which is attributed to acyl C–O(Coates, 2006). The peak at 1730 cm^{-1} in the ThL_{RIE} and $ThL_{RIE+Apt}$ spectrum is attributed to C=O stretching vibrations, indicating that the ThL electrodes were successfully functionalized with carboxylic groups(Coates, 2006). The FTIR spectrum for $ThL_{RIE+Apt}$ shows an apparent peak at 1571 cm^{-1}, which is related to the amide II bond and represents covalent bonding affinity aptamers on the surfaces of the ThL electrodes(Choi et al., 2010). The FTIR results confirm that the oxygen plasma oxidation treatment was a simple yet effective means for generating reactive surfaces with the high possibility of covalent bonding of PDGF-BB binding aptamers on ThL electrode surfaces.

3.2. Electrochemical analysis of ThL electrodes

In this section, electrochemical analyses of C-MEMS electrodes after each stage of development are presented. These analyses aimed to confirm the successful immobilization of aptamers and binding of target molecules on aptasensor surfaces. Two hypotheses for designing the aptasensors were considered: first, the formation of a PDGF-BB oncoprotein-aptamer complex (i.e., capturing the target molecules) increases the charge-transfer resistance by hindering the access of redox species to the surface of the aptasensor. Second, the formation of this complex diminishes the double-layer capacitance (i.e., charge density), which can be traced by calculating the areal capacitance from CV measurements as well as evaluating the double-layer capacitance from EIS measurements. The EIS measurements were conducted in the Faradaic mode (E = 0.35 V vs. Ag/AgCl) and non-Faradaic mode ($E = E_{OC}$) to measure the charge-transfer resistance and the double-layer capacitance, respectively. The 500 pM PDGF-BB was used as the sample target (referred to as T). Randles equivalent circuit (Fig. S1) was used to evaluate the charge-transfer resistance values from EIS measurements. This circuit was composed of R_s, C_{DL}, R_{CT}, and Z_W, representing the solution resistivity, the double-layer capacitance, the charge-transfer resistance, and impedance of the cell in low frequencies (i.e., Warburg impedance), respectively. The Faradaic path was modeled with R_{CT} and Z_W and non-Faradaic path was modeled with C_{DL}(Uygun and Uygun, 2014). Furthermore, the assumption on the reversibility of oxidation/reduction of $Fe(CN_6)^{-3/-4}$ redox couple was validated by measuring the CV responses with various scan rates.

The results of the EIS characterization of ThL_{Bare}, ThL_{RIE}, $ThL_{RIE+Apt}$, and responses of $ThL_{RIE+Apt}$ electrodes to 500 pM PDGF-BB are represented in Fig. 3A. The Nyquist plot of ThL_{Bare} has a small semi-circle radius compared to the others, which indicates a small R_{CT} of 72.01 Ω and good conductivity of the ThL_{Bare} electrode. ThL_{RIE} electrode has a higher R_{CT} of 152.18 Ω compared to the ThL_{Bare}, which is due to the negatively charged carboxylate group covering the surface of ThL_{RIE}.

The immobilization of aptamers slightly decreased the R_{CT} to a value of 114.9 Ω, which could be the result of the engagement of carboxylate groups of the surface in amide bonding (i.e., covalent immobilization of aptamers) and quenched remaining carboxyl groups by Tween-20 quencher. The $ThL_{RIE+Apt}$ electrode incubated with target molecules ($ThL_{RIE+Apt}$ + T) has a considerably high R_{CT} of 1423.9 Ω, which is a result of the isolative properties of the target and reduced access of the

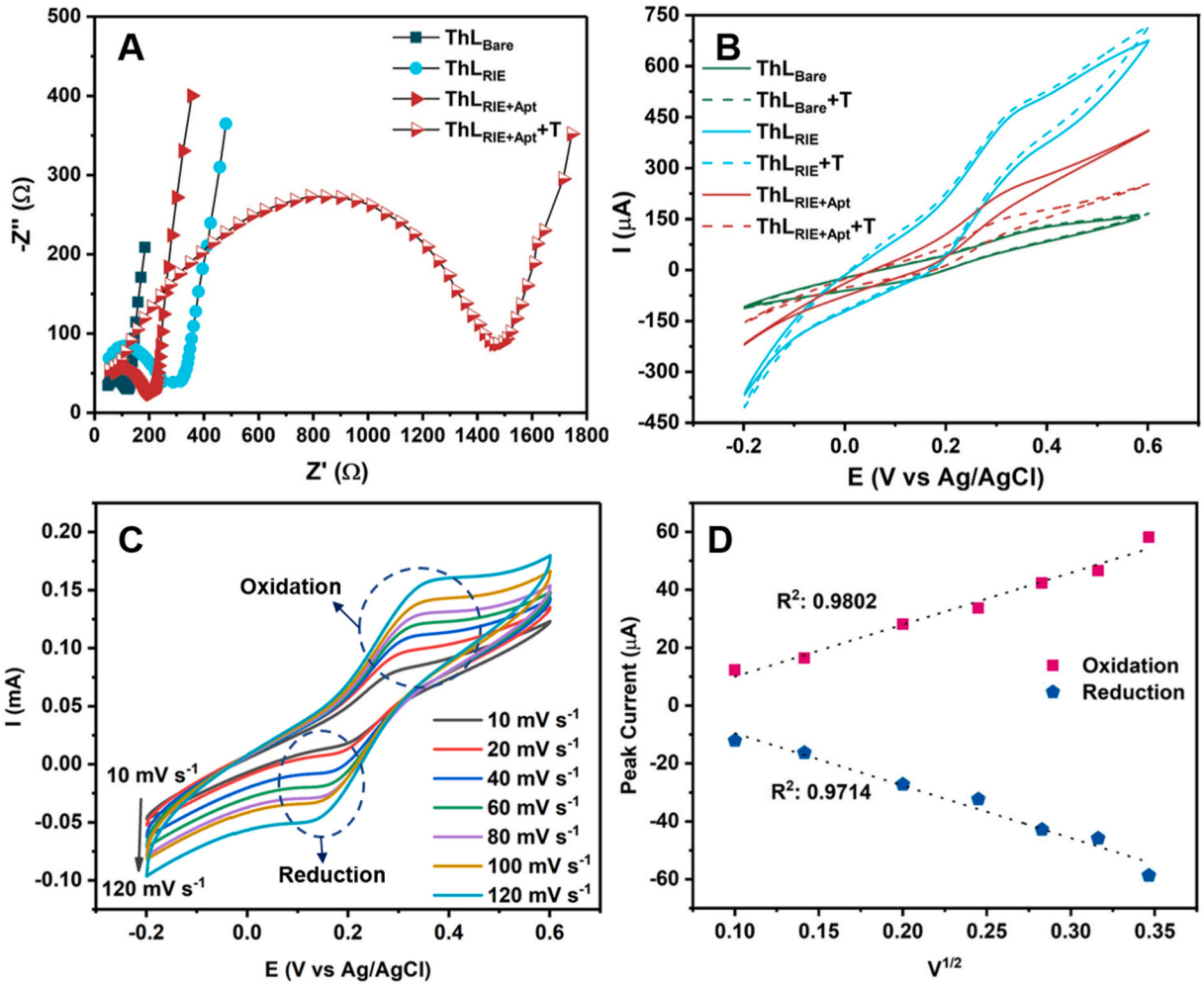

Fig. 3. A) The Nyquist plots of ThL electrodes at various stages of development and response of the $ThL_{RIE+Apt}$ electrode to 500 pM PDGF-BB. B) The CV responses of ThL_{Bare}, ThL_{RIE}, and $ThL_{RIE+Apt}$ electrodes to 500 pM PDGF-BB. C) The CV curves of the $ThL_{RIE+Apt}$ electrode at various scan rates ranging from 10 to 120 mV s^{-1}. D) The calibration curves of oxidation and reduction peak current versus the square root of scan rates.

charged species to the surface of the sensing electrodes(Liu et al., 2015). Furthermore, the EIS response of ThL_{Bare}, ThL_{RIE}, and $ThL_{RIE+Apt}$ electrodes to PDGF-BB measurement was explored. As the EIS results (Fig S2) show, the R_{CT} of ThL_{Bare} and $ThL_{RIE,}$ did not change after incubation with PDGF-BB, while $ThL_{RIE+Apt}$ showed the response mentioned earlier. Thus, the EIS characterization of C-MEMS electrodes confirmed that PDGF-BB oncoproteins were successfully captured on the surfaces of the aptasensor, and that capturing the PDGF-BB oncoproteins increases the R_{CT}.

The results of the CV measurements, which were designed to examine the second hypothesis and validate the efficiency of CV measurements, are shown in Fig. 3B. The curves represent the CV characteristics of the ThL_{Bare}, ThL_{RIE}, $ThL_{RIE+Apt}$, and their response to 500 pM PDGF-BB. ThL_{Bare} and ThL_{RIE} electrodes showed no response to PDGF-BB; the areal capacitance of ThL_{Bare} remained 6.05 mF cm^{-2} after target incubation, and the areal capacitance of ThL_{RIE} showed a negligible change of 23.38 to 22.34 mF cm^{-2} after target incubation. The area of CV curve of the $ThL_{RIE+Apt}$ electrode after PDGF-BB incubation showed a noticeable decrease. The binding of PDGF-BB oncoproteins decreased the areal capacitance of the $ThL_{RIE+Apt}$ electrode from 14.14 to 7.24 mF cm^{-1}. This change indicates that the aptamers were able to capture the target molecules successfully, and that CV measurement is sensitive to the captured PDGF-BB oncoproteins. Furthermore, the second hypothesis was investigated by studying the fitting value of C_{DL} measured at non-Faradaic mode (i.e., at $E = E_{OC}$). The calibration curve of C_{DL} fitting values (Fig. S2) reveals a declining linear response to the logarithm of PDGF-BB concentration with a slope of -5.02×10^{-7} Ω $Logc^{-1}$ (unit of c, nM) and correlation coefficient (R^2) of 0.8488. Both CV and EIS results validate the second hypothesis regarding responses of C-MEMS electrodes to target molecules.

In order to investigate the reversibility of the oxidation/reduction of $Fe(CN)_6^{-3/-4}$ and the ohmic drop, a set of CV measurements with different scan rates was conducted on $ThL_{RIE+Apt}$ electrodes. The CV curves of $ThL_{RIE+Apt}$ measured in different scan rates in the range of 10–120 mV s^{-1} are shown in Fig. 3C, indicating the oxidation and reduction peak currents found to be linearly proportional to the square root of the scan rates in the range of 10–120 mV s^{-1} with R^2 of 0.9802 and 0.9714 for oxidation peak currents and reduction peak currents, respectively (Fig. 3D). This linear correlation indicates that a diffusion-controlled process occurred on the $ThL_{RIE+Apt}$ electrodes. Hence, the Randles-Sevcik equation (Eq. (2)) was used to calculate the electrochemically active surface area of the $ThL_{RIE+Apt}$ electrodes at room temperature (T = 295 K)(Allen and Larry, 2001).

$$I_P = \left(2.69 \times 10^5\right) n^{3\backslash 2} A C D^{1/2} \nu^{1/2} \quad (2)$$

Where n is electron transfer number ($n = 1$), A is active surface area (cm^{-2}), C is the concentration of $Fe(CN)_6^{-3\backslash -4}$ (5 mol cm^{-3}), D is the diffusion coefficient of 5 mM $Fe(CN)_6^{-3/-4}$ (7.6×10^{-6} cm^2 s^{-1}), and ν is the scan rate (V s^{-1}). The active surface area was calculated as 0.0313 cm^2 with a STDEV of 0.00193.

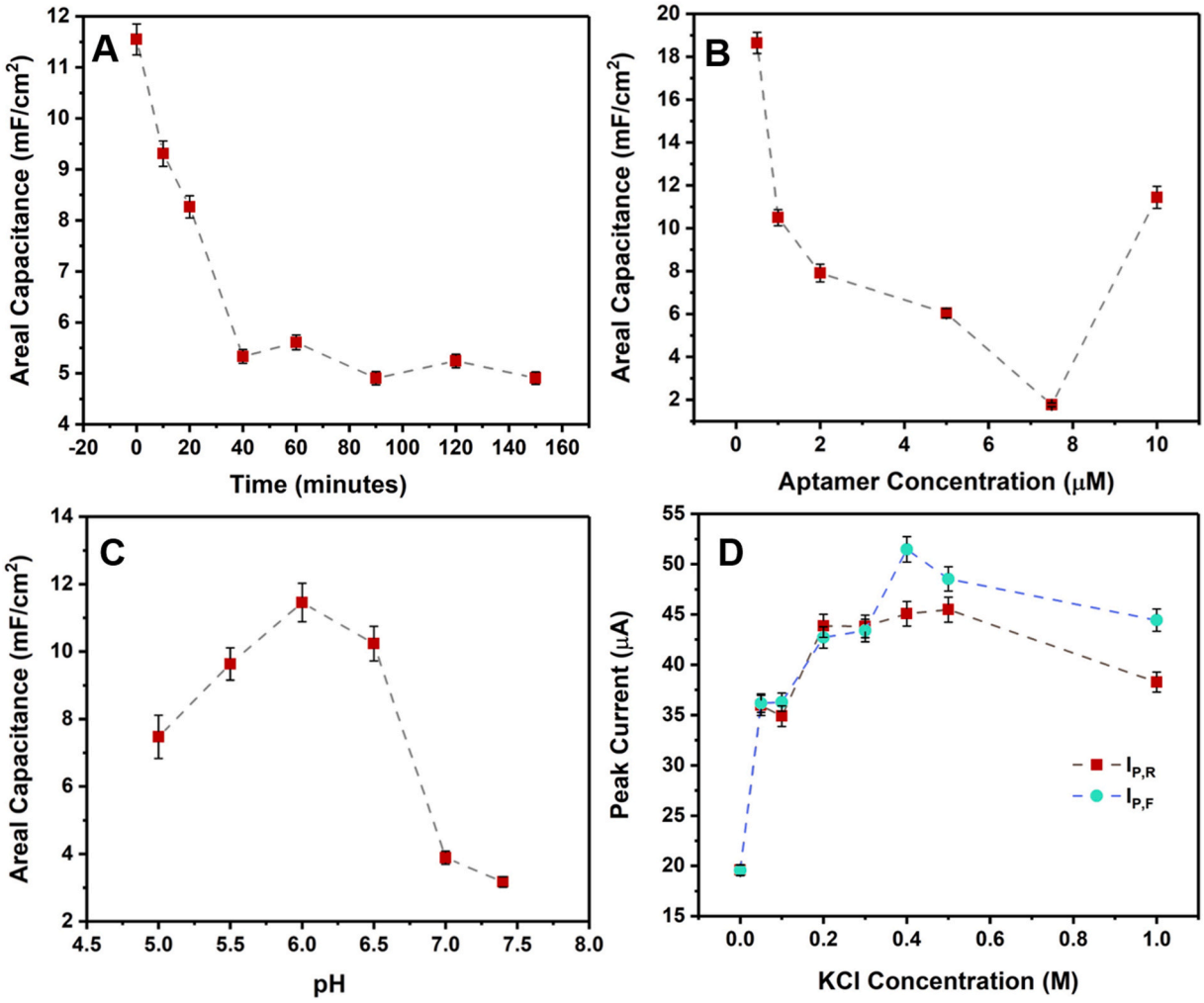

Fig. 4. A) Areal capacitances calculated from CV curves measured for 500 pM PDGF-BB to study the effect of reaction times. B) Areal capacitances calculated from CV curves measured for 500 pM PDGF-BB to study the effect of aptamer concentration. C) Areal capacitances calculated from CV curves measured for 500 pM PDGF-BB in electrolytes with different pH. D) The oxidation peak currents ($I_{P,F}$) and reduction peak currents ($I_{P,R}$) measured via CV vs. KCl concentration ranging from 0 to 1 M.

The charge transfer coefficient (α) for a similar system was assumed to be 0.5(Hajian et al., 2017). The α was calculated experimentally using Eq. (3)(Allen and Larry, 2001).

$$E_P - E_{P/2} = \ 48/\alpha n \tag{3}$$

Where E_P (mV) is the voltage of peak current and n is electron transfer number ($n = 1$). The value of α for oxidation reactions was found to have an average of 0.41 with STDEV of 0.0172. The theoretical and experimental values are slightly different, but this difference is insignificant since the experimental value lies in the reversible zone (Allen and Larry, 2001).

The Nicholson method based on peak potential separation (Eq. (4)) was used for evaluating the standard heterogeneous electron transfer rate constant (k^0)(Nicholson and Shain, 1964).

$$k^0 = 2.18\left[\frac{\alpha D n F \nu}{RT}\right]^{1/2} \exp\left[\frac{-\alpha^2 n F\left(E_{P,O} - E_{P,R}\right)}{RT}\right] \tag{4}$$

Where α was calculated from Eq. (3), D is the diffusion coefficient of 5 mM $Fe(CN)_6^{-3/-4}$ (7.6×10^{-6} $cm^2\ s^{-1}$), F is Faraday constant (96,485.34 C mol^{-1}), ν is scan rate (V s^{-1}), R is the universal gas constant (8.3145 J mol^{-1} K^{-1}), T is room temperature (295 K), $E_{P,O}$ and $E_{P,R}$ are oxidation and reduction peak potential, respectively(Allen and Larry, 2001). The calculated standard heterogeneous electron transfer rate constants (k^0) had an average of 0.00036 cm s^{-1} and STDEV of 0.00006 with the highest value at the scan rate of 50 mV s^{-1}.

Furthermore, the highest oxidation to the reduction peak currents had a ratio of 1.015, which indicates a reversible reaction(Aristov and Habekost, 2015). The peak-to-peak separation values in each scan rate had a STDEV of 0.008 V, which indicates that the reaction was reversible and the adsorption of redux species on the surface of $ThL_{RIE+Apt}$ was negligible. Moreover, the small variation in peak-to-peak separation indicated the small ohmic drop of solution(Aristov and Habekost, 2015; Elgrishi et al., 2018).

3.3. Optimization of fabrication and sensing conditions

Several factors are known to affect the performance of electrochemical aptasensors(Forouzanfar et al., 2020b). In this study, we have analyzed the effects of four parameters on responses of C-MEMS aptasensors, including reaction-time, binding aptamer concentration, pH of the electrolyte, and concentration of supporting salt (i.e., KCl). It worth noting that the temperature of the target incubation can also affect the sensing performance of the aptasensors(Ilgu and Nilsen-Hamilton, 2016). In designing the C-MEMS based aptasensors, it was envisioned that the aptasensing unit would be integrated with temperature control units to ensure that the aptasensor performs at its optimized condition.

Reaction time in aptasensors is referred to as the minimum time

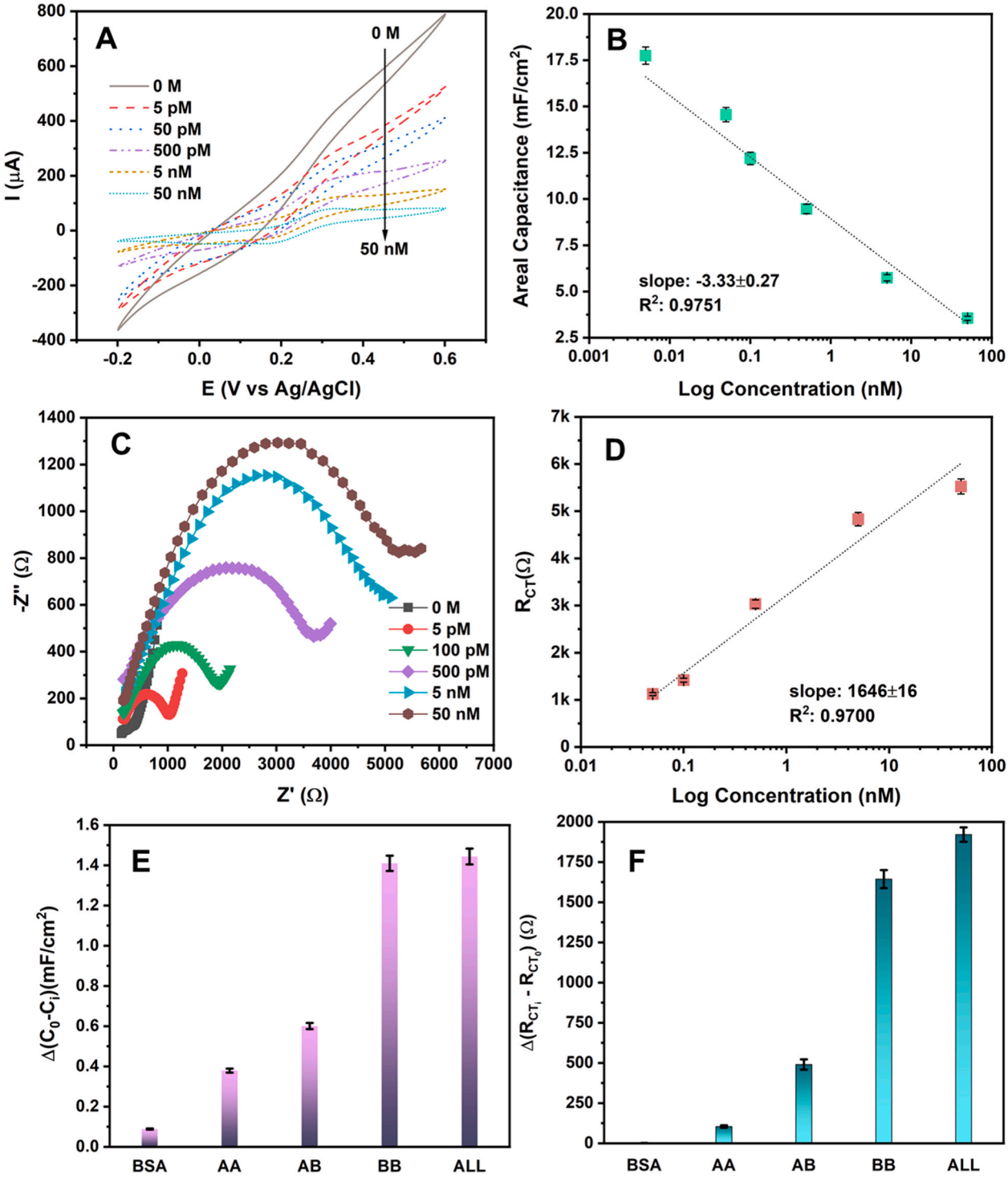

Fig. 5. A) CV curves of the $ThL_{RIE+Apt}$ electrode's response to PDGF-BB ranging from 0 to 50 nM. B) Calibration curve for calculated areal capacitances from CV curves with $n = 5$. C) EIS Nyquist plots of the $ThL_{RIE+Apt}$ electrode's response to PDGF-BB ranging from 0 to 50 nM. D) Calibration curve for R_{CT} extracted from Nyquist plots with $n = 5$. E) Areal capacitances calculated from CV curves and F) R_{CT} calculated from EIS Nyquist plot measured in response of $ThL_{RIE+Apt}$ electrodes to 4 μg mL^{-1} BSA. 50 nM PDGF-AA, 50 nM PDGF-AB, and 500 pM PDGF-BB and all the interference agents added to 500 pM PDGF-BB (designated as ALL).

required for the formation of the aptamer-target complex, and it depends predominantly on the DNA features (e.g., the length of the DNA sequence) (Forouzanfar et al., 2020b). As expected, longer reaction times (i.e., incubation) result in better detection efficiency. This optimization aimed to define the reaction time that is both quick and sufficiently efficient. To investigate the effect of reaction time, the $ThL_{RIE+Apt}$ electrodes were incubated with the target for various periods ranging from 10 to 150 min and tested by measuring the areal capacitance calculated from the CV curves using Eq. (1). The results are presented in Fig. 4A with the error bars calculated for $n = 3$ measurements. As shown, the areal capacitances decrease by increasing the reaction up to 40 min and saturate afterward. Hence, 40 min was chosen as the optimum reaction time.

In this study, we recorded the capacity values after the redox

reaction fully completed, so that the concentration of the aptamer stock solution was simply considered as the aptamer concentration. For each aptamer concentration ranging from 0.5 to 10 μM, a separate $ThL_{RIE+Apt}$ electrode was used. The areal capacitances were calculated from CV measurements conducted on $ThL_{RIE+Apt}$ electrodes using Eq. (1) for $n = 3$ measurements. As shown in Fig. 4B, the $ThL_{RIE+Apt}$ electrode exhibits its peak capacitive response at the aptamer concentration of 7.5 μM. The likely reason for the observed bell-shaped plot on the effect of aptamer concentration is the reduced amount of immobilized affinity aptamers above a certain concentration, due to repealing of the DNA molecules by other DNA molecules, since DNA molecules are negatively charged because of their phosphate groups(Manning, 1978). Consequently, the reduced amount of immobilized binding aptamers lessens the areal capacitance change in response to PDGF-BB, which can be seen as an increased value of areal capacitance after 7.5 μM aptamer concentration. Based on the results, the optimum aptamer concentration of 7.5 μM was used for the fabrication of C-MEMS aptasensors.

The optimum pH for electrochemical measurement was studied by measuring CV responses of $ThL_{RIE+Apt}$ electrodes to 500 pM PDGF-BB measured in the electrolyte of 0.1 M PBS/0.2 M KCl/5 mM $K_3Fe(CN)_6$ at different pH ranging from 5 to 7.5. As shown in Fig. 4C, the highest response was recorded at pH 6.5. Hence, pH 6.5 was used for sensing measurements.

The effect of supporting salt in the electrolyte on electrochemical measurements was studied by conducting CV measurements on $ThL_{RIE+Apt}$ in electrolytes with different KCl concentrations varying from 0 to 1 M. As the results represented in Fig. 4D show, the forward (oxidation) peak current (designated as $I_{P,F}$) and reverse (reduction) peak current (designated as $I_{P,R}$) increase proportionally by increasing the KCl concentration up to 0.2 M. Further increasing the KCl concentration did not affect the $I_{P,R}$. At the same time, the $I_{P,F}$ continued its increase up to 0.4 M KCl concentration. The correlation of $I_{P,F}$ and $I_{P,R}$ shows that the oxidation and reduction of $Fe(CN)_6^{-3/-4}$ was reversible up to 0.3 M KCl, and further increasing KCl concentration made the reaction irreversible. By considering the observed saturation point for $I_{P,R}$, the optimum KCl concentration of 0.2 mM was used for sensing performance characterizations.

3.4. Sensing performances of PDGF-BB aptasensors

The turn-off and turn-on strategies can apply to label-free electrochemical aptasensors in a similar manner to optical aptasensors(Benvidi et al., 2018; Shamsipur et al., 2015). In this study, the turn-off strategy was designed based on measuring areal capacitances using CV measurements. Likewise, the turn-on strategy was designed based on measuring R_{CT} via EIS measurements in the Faradaic mode.

The turn-off responses of the C-MEMS aptasensor measured for $ThL_{RIE+Apt}$ in response to 0–50 nM PDGF-BB are presented in Fig. 5A. The oxidation of peak $Fe(CN)_6^{-3/-4}$ at E = 0.3V (vs. Ag/AgCl) was decreased proportionally to the increase of the PDGF-BB concentration. The observed decrease in the peak current is the result of increased R_{CT} of the sensing probe. The calibration curve for calculated areal capacitances using Eq. (1) is shown in Fig. 5B. The calibration curve was obtained by calculating the average value of areal capacitances (mF cm^{-2}) from the responses of optimized $ThL_{RIE+Apt}$ aptasensor with the repeated measurements of $n = 5$. The area under the CV curves decreased substantially upon increasing the PDGF-BB concentrations. The decrease in the areal capacitance (charge density) suggests that the PDGF-BB oncoproteins were successfully attached to the $ThL_{RIE+Apt}$ surface and displaced the double-layer(Liu et al., 2015). The linear dependence of the output capacitance on the logarithm of PDGF-BB concentration has a slope of −3.33 mF cm^{-2} $Logc^{-1}$ (unit of c, nM) and the R^2 of 0.9751. The correlation of $ThL_{RIE+Apt}$ capacitance to the logarithm of PDGF-BB concentration can be assessed as following (Eq. (5)),

$$C = 8.93 - 3.33\ \ Logc^{-1},\ r = 0.9688 \tag{5}$$

where C is the areal capacitance (mF cm^{-2}), c is the PDGF-BB concentration (nano-mol L^{-1}) and r is the regression coefficient. Hence, the CV measurement's sensitivity to PDGF-BB can be calculated as 3.33 mF cm^{-2} $Logc^{-1}$ (unit of c, nM). The limit of detection (LoD) for $ThL_{RIE+Apt}$ aptasensors based on CV measurements was calculated as 7 pM based on the linear regression (Eq. (6)) (Shrivastava and Gupta, 2011),

$$LoD = \frac{3S}{b} \tag{6}$$

where S is the standard deviation of the blank response (STDEV = 0.0353 mF cm^{-2}, n=9), and b is the slope of the calibration curve (b = −13.82 mF cm^{-2} c^{-1} (unit of c, nM) of areal capacitances.

The turn-on responses of C-MEMS aptasensors measured for $ThL_{RIE+Apt}$ in response to 0–50 nM PDGF-BB are represented in Fig. 5C. The EIS data were recorded at the $E = E_{oxidation}$ (vs. Ag/AgCl), which was defined by conducting CV measurements intended to measure the R_{CT} in Faradaic mode. The radius of semi-circles in Nyquist plots, which represents the *resistivity of solution* + R_{CT}, increased proportionally to the increase of PDGF-BB. The increase of R_{CT} can be explained by target molecule isolative properties(Liu et al., 2015). The aforementioned equivalent circuit (Fig. S1) was used for obtaining the values of R_{CT} in which a good match between the fitting curves and measured curves was observed (Table S1). The calibration curve of R_{CT} measured for each concentration of PDGF-BB with repeated measurements of $n = 5$ is presented in Fig. 5D. The linear dependence of the R_{CT} on the logarithm of PDGF-BB concentration has a slope of 1.65×10^3 Ω $Logc^{-1}$ (unit of c, nM) and R^2 of 0.9700. The correlation of R_{CT} to the logarithm of PDGF-BB concentration can be assessed as following (Eq. (7)),

$$R_{CT} = 3.22 \times 103 + 1.65 \times 10^3 Logc^{-1},\ r = 0.9604 \tag{7}$$

where R_{CT} is charge transfer resistance (Ω), c is the PDGF-BB concentration (nano-mol L^{-1}), and r is the regression coefficient. The EIS measurement's sensitivity to PDGF-BB is found to be 1.65×10^3 Ω $Logc^{-1}$ (unit of c, nM). The LoD for $ThL_{RIE+Apt}$ aptasensors based on EIS measurements was calculated as 1.9 pM based on linear regression (Eq. (6)) in which S (i.e., STDEV) was calculated as 2.39 Ω (n=20), and b was calculated as 4.16×10^3 Ω c^{-1} (unit of c, nM).

Both detection strategies were found to be sensitive to PDGF-BB with a wide range of linear response. This result demonstrated that the turn-on strategy established lower LoD compared to the LoD for turn-off strategy measurements. The difference in LoD achieved by turn-on and turn-off strategies could be a result of the difference in the essence of CV and EIS measurements, as well as considered assumptions for calculating the areal capacitance and R_{CT}.

3.5. Analytical parameters of PDGF-BB aptasensors

In this study, four analytical parameters of selectivity, storage stability, repeatability, and robustness of C-MEMS PDGF-BB aptasensor were evaluated. The selectivity of the $ThL_{RIE+Apt}$ aptasensors was studied by measuring the response of the aptasensors to 4 μg mL^{-1} BSA, 50 nM PDGF-AB, and 50 nM PDGF-AA along with 500 pM PDGF-BB. The concentrations of interference agents were chosen to be approximately 100 times higher than concentrations of the target molecules. The results of the selectivity measurements are presented in Fig. 5E and F in which the areal capacitances (Fig. 5E) and R_{CT} (Fig. 5F) were calculated from the CV curves and EIS Nyquist plots and differentiated from their blank responses, respectively.

The capacitive response of $ThL_{RIE+Apt}$ aptasensors to PDGF-BB was 3.72 and 2.34 times higher than that of the aptasensors to PDGF-AA and PDGF-AB, respectively. Likewise, the resistive response of $ThL_{RIE+Apt}$ aptasensors to PDGF-BB was 15.79 and 3.35 times higher than that of the aptasensors to PDGF-AA and PDGF-AB, respectively. Furthermore, the normalized responses of the label-free C-MEMS aptasensor to interference agents are represented in Fig. S4, which shows the superior

Table 1
Comparison of recent electrochemical PDGF-BB aptasensors.

Substrate	Active Electrode	Labeling	Measurement Technique/ Parameter	Linear Range	LoD	Ref.
Au	graphene doped with silver nanoclusters	label-free	EIS/R_{CT}	32.3 fM–1.61 pM	26.5 fM	Zhang et al. (2017)
glassy carbon	graphene/multi walled carbon nanotubes doped with Se	label-free	differential pulse voltammetry/current	0.1 pM-10 nM	27 fM	Wang et al. (2018)
glassy carbon	hydroxyapatite nanoparticles	labeled: hydroxyapatite nanoparticles	square wave voltammetry/ current	0.1 pg mL^{-1}-10 ng mL^{-1}	50 fg mL^{-1}	Jiang et al. (2017)
glassy carbon	molybdenum selenide–graphene	labeled: exonuclease III	differential pulse voltammetry/current	0.0001–1 nM	20 fM	Huang et al. (2016)
N/A	catalytic-induced DNA hydrogel	labeled: C_3N_4/Au/Fc-NH_2	square wave voltammetry/ current	0.01 pM-10 nM	3.5 fM	Chang et al. (2018)
glassy carbon	MoS_2/carbon/gold nanoparticles aerogel composites	labeled: 6-ferrocenyl hexanethiol	differential pulse voltammetry/current	0.001–10 nM	0.3 pM	Fang et al. (2015)
SiO_2	carboxyl functionalized photoresist derived carbon	label-free	CV/capacitance EIS/R_{CT}	0.0–50 nM and 0.005–50 nM	7 pM and 1.9 pM	current study

selectivity response of the resistance detection method over the capacitance detection method. The selectivity studies suggest that the EIS technique offers more accurate results for label-free C-MEMS based PDGF-BB aptasensors.

The storage stability of PDGF-BB aptasensors was evaluated by repeating the electrochemical measurements on $ThL_{RIE+Apt}$ in response to 500 pM PDGF-BB every two days until the recorded response was less than 50% of the initial response. The capacitive response (9.03 mF cm^{-1}) of ThL aptasensor to 500 pM PDGF-BB after 10 days was 90.34% of the initial capacitive response (9.99 mF cm^{-1}), which indicates that the developed aptasensor has a sufficiently long lifetime and storage stability. The repeatability of the label-free C-MEMS based PDGF-BB aptasensors was investigated by analyzing the CV response of several ($n = 8$) similarly prepared $ThL_{RIE+Apt}$ electrodes to 500 pM PDGF-BB (Fig. S5). The repeatability CV tests resulted in STDEV of 0.6055 mF cm^{-2} with an average value of 8.1982 mF cm^{-2}, illustrating the excellent repeatability of developed aptasensors.

Biosensor robustness is defined as the capability of the biosensor to remain unaffected by small but deliberate deviations in the methodology parameters(Ermer and Miller, 2006). In order to study the robustness of the C-MEMS PDGF-BB aptasensor, a $ThL_{RIE+Apt}$ electrode was heated to 50 °C during several ($n = 8$) regeneration steps to determine the capability of the biosensor to recover its initial state. The areal capacitance calculated from CV measurements after each heating step showed an average of 10.59 mF cm^{-2}, which was 88.5% of initial response (11.96 mF cm^{-2}) with STDEV of 0.6093. Thus, the oxygen-plasma treated C-MEMS electrodes were proven to be highly robust platforms for label-free electrochemical PDGF-BB aptasensors.

Table 1 compares the current PDGF-BB aptasensor with other, recently developed electrochemical PDGF-BB aptasensors. The linear ranges attained via both CV and EIS techniques show noticeable improvement in comparison to both labeled and label-free PDGF-BB electrochemical aptasensors. The linear range sufficiently covers the ranges of PDGF-BB in healthy humans as well as most patients with cancer diseases. Moreover, by considering 0.1 ng mL^{-1} (the equivalent of 41 pM) as the minimum cut off point for normal range of PDGF-BB in human serums, $ThL_{RIE+Apt}$ aptasensors exhibited adequate LoD and sensitivity(Leitzel et al., 1991).

The further enhancement can be deployed for C-MEMS based PDGF-BB aptasensors. For instance, the 3D structured C-MEMS devices can be used for sensing platforms in which the enhanced resolution can increase the aptamer loading efficiency. Moreover, the integration of carbon-based nanomaterials (e.g., graphene nanosheets) and C-MEMS devices can enhance the performance of the aptasensors by increasing the accessible surface area and specific capacitances(Penmatsa et al., 2012). Additionally, the results of this study illustrate the superior performance of the EIS technique (i.e., resistivity measurements) compared to the CV technique (i.e., areal capacitance measurements) for the developed label-free electrochemical C-MEMS aptasensor; consequently, the EIS technique is suggested for future POC device development.

4. Conclusion

In this study, a novel method was used to covalently immobilize PDGF-BB affinity aptamers on the surface of C-MEMS electrodes. Oxygen-plasma treatment was used to introduce carboxyl groups to the surface of C-MEMS electrodes. The carboxyl groups covered the surface of C-MEMS, thus enabling highly efficient and stable immobilization of the PDGF-BB affinity aptamers. The technique for fabrication of label-free electrochemical cancer aptasensors described herein has great mass-production potential, promising a large fabrication yield of highly stable devices by virtue of the repeatability of the synthesizing procedure (i.e., photolithography and high-temperature carbonization) and the oxygen-plasma treatment. Both turn-off and turn-on strategies provided sensitive and selective sensing measurements; however, EIS measurement provided more sensitive and selective responses than the CV technique. The highly sensitive, selective, and stable label-free electrochemical PDGF-BB aptasensor detailed herein demonstrates that the C-MEMS platform is highly promising for developing reliable, precise, and feasible aptasensors for point-of-care and early detection of cancer.

CRediT authorship contribution statement

Shahrzad Forouzanfar: Conceptualization, Methodology, Validation, Formal analysis, Writing - original draft, Visualization, Writing - review & editing. **Fahmida Alam:** Data curation, Writing - review & editing. **Nezih Pala:** Writing - review & editing, Supervision. **Chunlei Wang:** Writing - review & editing, Supervision, Funding acquisition.

Declaration of competing interest

The authors declare that they have no known competing financial interests or personal relationships that could have appeared to influence the work reported in this paper.

Acknowledgments

This work was supported by the National Science Foundation (NSF) projects with the award nos. 1611088 and 1648451. The authors wish to thank Thomas Fieldsend for his technical and grammatical revisions to the manuscript.

Appendix A. Supplementary data

Supplementary data to this article can be found online at https://doi.

org/10.1016/j.bios.2020.112598.

References

Adelowo, E., Baboukani, A.R., Okpowe, O., Khakpour, I., Safa, M., Chen, C., Wang, C., 2020. J. Power Sources 455, 227987.
Allen, J.B., Larry, R.F., 2001. John Wiley & Sons.
Aristov, N., Habekost, A., 2015. World J. Chem. Educ 3 (5), 115–119.
Benvidi, A., Banaei, M., Tezerjani, M.D., Molahosseini, H., Jahanbani, S., 2018. Microchimica Acta 185 (1), 50.
Cao, R., Björndahl, M.A., Religa, P., Clasper, S., Garvin, S., Galter, D., Meister, B., Ikomi, F., Tritsaris, K., Dissing, S., 2004. Canc. Cell 6 (4), 333–345.
Chang, Y., Li, M., Wu, Z., Zhuo, Y., Chai, Y., Xiao, Q., Yuan, R., 2018. Anal. Chem. 90 (13), 8241–8247.
Chatterjee, S.K., Zetter, B.R., 2005. Future Oncol. 1 (1), 37–50.
Cheng, J., Ye, H., Liu, Z., Xu, C., Zhang, Z., Liu, Y., Sun, Y., 2013. J. Cell. Biochem. 114 (7), 1510–1518.
Choi, E.-Y., Han, T.H., Hong, J., Kim, J.E., Lee, S.H., Kim, H.W., Kim, S.O., 2010. J. Mater. Chem. 20 (10), 1907–1912.
Cimpean, A.M., Cobec, I.M., Ceausu, R.A., Popescu, R., Tudor, A., Raica, M., 2016. CANCER GENOMICS PROTEOMICS 13 (6), 511–517.
Coates, J., 2006. John Wiley & Sons, 9780471976707.
Cui, L., Lu, M., Li, Y., Tang, B., Zhang, C.-y., 2018. Biosens. Bioelectron. 102, 87–93.
Elgrishi, N., Rountree, K.J., McCarthy, B.D., Rountree, E.S., Eisenhart, T.T., Dempsey, J. L., 2018. J. Chem. Educ. 95 (2), 197–206.
Ermer, J., Miller, J.H.M., 2006. John Wiley & Sons.
Fang, L.-X., Huang, K.-J., Liu, Y., 2015. Biosens. Bioelectron. 71, 171–178.
Ferrer-Argemi, L., Aliabadi, E.S., Cisquella-Serra, A., Salazar, A., Madou, M., Lee, J., 2018. Carbon 130, 87–93.
Forouzanfar, S., Alam, F., Khakpour, I., Baboukani, A.R., Pala, N., Wang, C., 2020a. IEEE Sensor. J. 20 (16), 8965–8972.
Forouzanfar, S., Alam, F., Pala, N., Wang, C., 2020b. J. Electrochem. Soc. 167 (6), 067511.
Forouzanfar, S., Talebzadeh, N., Zargari, S., Veladi, H., 2015. 2015 3rd RSI International Conference on Robotics and Mechatronics (ICROM). IEEE, pp. 629–634.
Frackowiak, E., 2007. Phys. Chem. Chem. Phys. 9 (15), 1774–1785.
Hajian, R., Tayebi, Z., Shams, N., 2017. Journal of pharmaceutical analysis 7 (1), 27–33.
Huang, K.-J., Shuai, H.-L., Zhang, J.-Z., 2016. Biosens. Bioelectron. 77, 69–75.
Ilgu, M., Nilsen-Hamilton, M., 2016. Aptamers in analytics Analyst 141 (5), 1551–1568.
Jannetto, P., 2017. Mass Spectrometry for the Clinical Laboratory. Elsevier, pp. 165–179.
Jiang, W., Tian, D., Zhang, L., Guo, Q., Cui, Y., Yang, M., 2017. Microchimica Acta 184 (11), 4375–4381.
Kajizuka, M., Miyachi, T., Matsuzaki, H., Iwata, K., Shinmura, C., Suzuki, K., Suda, S., Tsuchiya, K.J., Matsumoto, K., Iwata, Y., 2010. Prog. Neuro Psychopharmacol. Biol. Psychiatr. 34 (1), 154–158.
Kawaguchi, J., Adachi, S., Yasuda, I., Yamauchi, T., Yoshioka, T., Itani, M., Kozawa, O., Moriwaki, H., 2012. Oncol. Rep. 27 (4), 935–939.
Lau, C.K., Yang, Z.F., Ho, D.W., Ng, M.N., Yeoh, G.C., Poon, R.T., Fan, S.T., 2009. Clin. Canc. Res. 15 (10), 3462–3471.
Leitzel, K., Bryce, W., Tomita, J., Manderino, G., Tribby, I., Thomason, A., Billingsley, M., Podczaski, E., Harvey, H., Bartholomew, M., 1991. Canc. Res. 51 (16), 4149–4154.
Liu, X., Shuai, H.-L., Huang, K.-J., 2015. Analytical Methods 7 (19), 8277–8284.
Ma, F., Wei, S.-h., Zhang, C.-y., 2019. Anal. Chem. 91 (12), 7505–7509.
Ma, R., Yang, Q., Cao, S., Liu, S., Cao, H., Xu, H., Wu, J., Feng, J., 2020. OncoTargets Ther. 13, 1883.
Manning, G.S., 1978. Q. Rev. Biophys. 11 (2), 179–246.
Nicholson, R.S., Shain, I., 1964. Anal. Chem. 36 (4), 706–723.
Pei, C., Liu, C., Wang, Y., Cheng, D., Li, R., Shu, W., Zhang, C., Hu, W., Jin, A., Yang, Y., 2020. Angewandte Chemie International Edition.
Penmatsa, V., Kawarada, H., Song, Y., Wang, C., 2014. Material Science Research India 11 (1), 1–8.
Penmatsa, V., Kim, T., Beidaghi, M., Kawarada, H., Gu, L., Wang, Z., Wang, C., 2012. Nanoscale 4 (12), 3673–3678.
Piñón, M.V., Benítez, B.C., Pramanick, B., Perez-Gonzalez, V.H., Madou, M.J., Martinez-Chapa, S.O., Hwang, H., 2017. Sensor Actuator Phys. 262, 10–17.
Prasad, A., Choi, J., Jia, Z., Park, S., Gartia, M.R., 2019. Biosens. Bioelectron. 130, 185–203.
Ranjan, R., Esimbekova, E.N., Kratasyuk, V.A., 2017. Biosens. Bioelectron. 87, 918–930.
Shamsipur, M., Farzin, L., Tabrizi, M.A., Molaabasi, F., 2015. Biosens. Bioelectron. 74, 369–375.
Shrivastava, A., Gupta, V., 2011. Chronicles Young Sci. 2 (1), 21–25.
Syahir, A., Usui, K., Tomizaki, K.-y., Kajikawa, K., Mihara, H., 2015. Microarrays 4 (2), 228–244.
Uygun, Z.O., Uygun, H.D.E., 2014. Sensor. Actuator. B Chem. 202, 448–453.
Wang, C., Jia, G., Taherabadi, L.H., Madou, M.J., 2005. Journal of microelectromechanical systems 14 (2), 348–358.
Wang, C., Madou, M., 2005. Biosens. Bioelectron. 20 (10), 2181–2187.
Wang, C., Taherabadi, L., Jia, G., Madou, M., Yeh, Y., Dunn, B., 2004. Electrochem. Solid State Lett. 7 (11), A435–A438.
Wang, Y.-H., Chen, Y.-X., Wu, X., Huang, K.-J., 2018. Colloids Surf. B Biointerfaces 172, 407–413.
Wang, Y., Luo, J., Liu, J., Sun, S., Xiong, Y., Ma, Y., Yan, S., Yang, Y., Yin, H., Cai, X., 2019. Biosens. Bioelectron. 136, 84–90.
World Health Organization, 2020. Cancer. https://www.who.int/health-topics/cancer#tab=tab_1.
Willner, I., Zayats, M., 2007. Angew. Chem. Int. Ed. 46 (34), 6408–6418.
Yi, B., Williams, P.J., Niewolna, M., Wang, Y., Yoneda, T., 2002. Canc. Res. 62 (3), 917–923.
Zhang, R., Rejeeth, C., Xu, W., Zhu, C., Liu, X., Wan, J., Jiang, M., Qian, K., 2019. Anal. Chem. 91 (11), 7078–7085.
Zhang, Z., Guo, C., Zhang, S., He, L., Wang, M., Peng, D., Tian, J., Fang, S., 2017. Biosens. Bioelectron. 89, 735–742.